ingegneria sismica
International Journal of Earthquake Engineering
Anno XLIII - Num. 2 - 2026

Real-time monitoring of stress and deflection under asymmetric loading in bridge construction based on machine vision

Zetao Li[1], *Jianhua Du*[1,2,3,*] *and Fei Wang*[1]

[1] Department of Railway Engineering, Shijiazhuang Institute of Railway Technology, Shijiazhuang, Hebei, 050041, China
[2] Intelligent Control Technology Innovation Center for Bridge and Tunnel Engineering Construction of Hebei Province, Shijiazhuang, Hebei, 050041, China
[3] Application Technology R&D Center of Bridge and Tunnel Intelligent Construction of Hebei Colleges, Shijiazhuang, Hebei, 050041, China

SUMMARY: *In this paper, machine vision technology with non-contact, high efficiency and automation is selected for bridge structure measurement, expecting to build a practical real-time monitoring method. Combined with the relationship between the camera coordinate system and the world coordinate system, the camera calibration is carried out to eliminate the error caused by image distortion and realize the correction of image distortion. On this basis, the SIFT feature point detection method is selected to extract and match the image features to form the image measurement algorithm based on machine vision. The finite element structure is built based on the location information of the key points of the bridge acquired by vision, and the overall stress distribution data of the bridge structure is calculated. Meanwhile, based on the on-site measurement data, the three-dimensional deformation data of the bridge structure is output to complete the measurement of the bridge deflection. In the practical application of machine vision-based stress calculation and deflection measurement method in River Gorge Bridge K, the maximum stress calculation of the bridge cantilever top plate is 14.18MPa and the maximum stress calculation of the bottom plate is 17.49MPa, which is close to the actual measurement results, and the difference between the deflection measurement of the bridge and the GPS measurement is less than 1mm, which shows a wide range of prospects for the application of stress and deflection monitoring on bridges.*

KEYWORDS: *finite element structure; machine vision; SIFT feature point detection; bridge structure; deflection measurement; stress monitoring*

1 Introduction

The rapid development of the current social economy and urbanization level makes the government and relevant departments pay more and more attention to the construction of infrastructure, in which the bridge construction project is a very important link in the construction of infrastructure, which bears an important responsibility for the safety of transportation. However, due to the rapid development of the transportation industry, bridge construction projects continue to increase, and at the same time for the quality of the construction process has higher requirements [1, 2]. Some of the existing bridge facilities have large spans, complex structures, and asymmetric loads in the construction process, and

*lizt_89@163.com
https://doi.org/10.65102/is2026659
Published: 30 April, 2026

in the process of its long-term use, the bridge structure is deformed and damaged, and some of the bridge structure has been unable to adapt to the current traffic flow, which seriously threatens the lives of the drivers and the safety of property [3-5]. Among them, asymmetric loading of bridge construction is a common phenomenon, due to the differences in bridge construction techniques lead to unbalanced loads on both sides or both ends of the bridge, or the differences in construction materials or uneven distribution of concrete caused by the difference in global stress, as well as construction equipment placed in the wrong location caused by the concentration of the local loads, which ultimately led to the deformation of the bridge structure is out of control, increasing the risk of construction [6-9]. In addition, during the bridge construction stage, the bridge may be disturbed by wind, rainfall, temperature changes and other environmental factors, resulting in the aggravation of local loads and uneven distribution of global loads, leading to the deterioration of long-term performance [10, 11]. Wu et al. [12] found that, during the design and construction stage of the bridge tilt-resistant structure, the bridge with unbalanced state is in a state of impact acceleration, rotational angular acceleration, the clearance between the support foot and the lower rotating platform, and the bridge displacement and stresses increase under the increased impact acceleration, rotation angle acceleration, support foot and lower rotating platform. Increase under the bridge displacement and stress gradually increased, increasing the bridge structural risk.

By monitoring the bridge construction process loads, structural deformation can be reduced, the service life of the bridge can be extended, and the operational safety of the bridge can be improved. Wang et al [13] proposed a feedback system for the construction monitoring of asymmetric prestressed concrete bridges with multi-line railroad crossings, combining a finite element analysis model to monitor and provide feedback on parameters such as maximum displacements, stresses, etc. during the construction to ensure the safety of the bridge construction. Li et al [14] used building information modeling technology to construct a safety analysis model for construction scenarios of prestressed concrete continuous girder bridges, and introduced a particle swarm optimization algorithm to optimize the model for safety analysis of main girder stresses in construction scenarios such as load imbalance, which is conducive to assisting in the monitoring of bridge construction. Gaute-Alonso et al [15] integrated a network of advanced force measurement sensors and synchronized multi-strain force measurement sensors to monitor stresses during two construction phases, active anchoring and short prestressing unit design, in the construction of large-span bridges, which improves the level of accuracy and control of stress measurements. Zheng et al [16] monitored the stresses, construction errors and safety status of arch bridge construction, and conducted static and dynamic load tests on the completed bridges to verify that the combination of stresses and deflection ranges under the foundation construction of pressurized arch bridges can meet the load bearing requirements. Zhang et al [17] used fiber-optic sensors to monitor the deflection changes in three key construction stages of long-span cantilever bridges, i.e., forward movement of hanging baskets, concrete pouring, and prestressing tensioning, and the monitoring results were consistent with the on-site conditions. The current stress and deflection monitoring during bridge construction is oriented to the whole construction process, and the stress and deflection under asymmetric loading of bridge construction are not carefully monitored and analyzed, and the monitoring method cannot meet the demand of real-time monitoring.

And machine vision has slowly evolved under the combined effect of long-term industrial automation needs, optical imaging technology, and the development of electronic computing. From the initial artificial visual assistance, to today's multimodal vision system widely used in manufacturing, transportation and other fields, it has experienced a continuous iteration from

low speed and low resolution to high speed and high resolution, and from local detection to global understanding [18-21]. Its core is not a single algorithm, but a whole set of system jointly supported by four elements: perception, imaging, illumination, processing and execution. Dan et al [22] used multi-source heterogeneous information from machine vision and weighing dynamic data fusion to construct a bridge group digital twin system, which acquires the bridge structural response data under load through sensors to realize the monitoring of bridge traffic loads. Zhao et al [23] proposed a highway bridge settlement monitoring technology based on machine vision, which can realize the real-time automatic monitoring of the bridge pile foundation displacement changes, and improve the safety guarantee for the bridge maintenance and construction during the pit excavation. Xie et al [24] carried out real-time monitoring of displacement and lateral deflection during the incremental lifting phase of bridge construction through machine vision technology, which introduced a target detection algorithm and a multi-target tracking model for detecting, recognizing, and tracking multi-targets during the construction phase. It can be seen that machine vision provides a new path for stress and deflection monitoring under load asymmetry in the bridge construction stage.

In this paper, based on the relationship between the camera coordinate system and the world coordinate system conversion, the calculation of the camera distortion coefficient, the correction method of image distortion under machine vision is proposed. SIFT feature point detection method is adopted for image feature extraction and matching, and an image measurement algorithm based on machine vision is established. Taking this algorithm as a measurement tool and combining with the actual situation of bridge construction, the finite element structural analysis method applicable to its stress structure distribution and the deflection measurement method are designed. The experimental samples are selected to observe and calculate the stress distribution and deflection performance by applying the method of this paper, so as to verify the technical support role of machine vision in the control of stress and deflection in bridge construction.

2 Machine Vision Based Image Measurement Algorithm

2.1 Camera Calibration and Aberration Correction

When measurement work is performed using machine vision, there are distortions between the camera-acquired image and the original spatial image. In order to obtain accurate spatial image information from the image, camera calibration is used to recognize and reconstruct spatial objects by extrapolating the geometric information of the objects in three-dimensional space from the image information acquired by the camera. The relationship between the real coordinates of a spatial object and the pixel coordinates of the corresponding points in the image captured by the camera is determined by the parameters of the geometric model of the camera imaging (camera parameters), and the process of solving the camera parameters is the camera calibration. Aberration correction is the process of using the solved parameters to restore the original information of the captured image.

The coordinate systems involved in the camera calibration process are shown in Figure 1, including the world coordinate system, the camera coordinate system, the image coordinate system and the pixel coordinate system. Camera calibration is the process of converting world coordinates into camera coordinates and then into image coordinates to eliminate the errors generated by aberrations in order to obtain accurate measurement results.

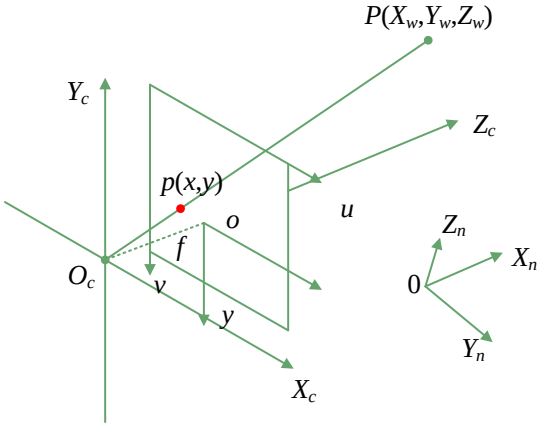

Figure 1: Four coordinate systems calibrated by the camera

The relationship between the world coordinate system and the image coordinate system for the point of the same name is obtained after two coordinate system transformations as in equation (1).

$$\begin{bmatrix} u \\ v \\ 1 \end{bmatrix} = K\begin{bmatrix} R|t \end{bmatrix}\begin{bmatrix} x \\ y \\ z \\ 1 \end{bmatrix} \tag{1}$$

u,v are the coordinates in the image coordinate system in mm; x, y, z are the coordinates in the world coordinate system in pixels; K is the camera internal reference, which is a 3*3 matrix whose function is to transform the coordinates from the camera coordinate system to the image coordinate system, and then to the pixel coordinates; R,t are the camera external references, and R is a 3*3 matrix representing the rotational transformation in the direction of x,y,z direction, and t is a 3*1 matrix representing the translation transformation in x,y,z direction.

Due to manufacturing accuracy and assembly deviations, the captured image may be distorted. Depending on the source of distortion, they are classified as radial and tangential distortion. Radial distortion is caused by the fact that when light passes through the center of the lens, light rays far from the center of the camera lens are more easily curved than light rays close to the center, resulting in pixel points that deviate close to or far from the center of the image plane, and the deviation gradually increases along the radius of the lens toward the outer circle. Tangential aberrations are due to the unevenness of the lens and the imaging plane causing probabilistic pixel deviation.

Radial aberrations as the target becomes farther away from the optical center position, the greater its effect on the imaging effect, in order to eliminate the effect of radial aberrations, the establishment of k_1,k_2,k_3 three coefficients, and expanded with Taylor series, can be expressed as equation (2).

$$\begin{cases} x = x'\left(1+k_1r^2+k_2r^4+k_3r^6\right) \\ y = y'\left(1+k_1r^2+k_2r^4+k_3r^6\right) \end{cases} \tag{2}$$

(x, y) are the image coordinates without aberration under the ideal optical center system, (x', y') are the image coordinates in the practical application, and r is the distance from the point to the imaging center.

With two parameters P_1 and P_2 to express the tangential distortion of the camera, the model of tangential distortion is expressed as equation (3).

$$\begin{cases} x = x' + \left[2P_1 x'y' + P_2(r^2 + 2x'^2) \right] \\ y = y' + \left[2P_2 x'y' + P_1(r^2 + 2y'^2) \right] \end{cases} \tag{3}$$

According to Eqs. (2) and (3), the superimposed combination of the two aberrations can eliminate the effects from both at the same time, and the parameter expression of the superposition is Eq. (4).

$$\begin{cases} x = x'(1 + k_1 r^2 + k_2 r^4 + k_3 r^6) + \left[2P_1 x'y' + P_2(r^2 + 2x'^2) \right] \\ y = y'(1 + k_1 r^2 + k_2 r^4 + k_3 r^6) + \left[2P_2 x'y' + P_1(r^2 + 2y'^2) \right] \end{cases} \tag{4}$$

Five aberration coefficients in camera calibration can be obtained in Eq. (4), i.e., radial aberration coefficients k_1, k_2, k_3, and tangential aberration coefficients P_1 and P_2. In the process of camera calibration, after obtaining the aberration parameter matrix, the corresponding point (x, y) under the ideal model is calculated for any output image point (x', y') according to Eq. (4), and the pixel point is assigned to (x', y') for further processing, and the pixel value of this point is calculated using interpolation if (x', y') is a non-integer, and a new pixel value is output when all pixel points have been processed, so as to realize the new image of image aberration. After all pixels are processed, a new image is output to realize the correction of image distortion.

2.2 Image feature extraction and matching

2.2.1 SIFT feature detection and feature point composition methods

The essence of the SIFT algorithm is to find the extreme points on different scale spaces and calculate the orientation elements and feature descriptors of the extreme points.The extreme point features found by SIFT are the points that will not change due to factors such as illumination, affine transformations and noise, etc.The main matching steps are as follows:

(1) Establish Gaussian difference pyramid

The scale recognized by the computer is the σ value of the two-dimensional Gaussian function, so when the image is convolved with a two-dimensional Gaussian function, many Gaussian images with different σ values can be obtained. For computers, the larger the Gaussian kernel, the more blurred the image, known as the “size space expression”, that is, in different Gaussian kernel smoothed by the different expression of the picture.SIFT algorithm in the two transformations of the image is shown in Figure 2(a)-(b). The multi-resolution expression of the image pyramid is a downsampling of the image, after downsampling the pixel points of the image will be reduced, the size of the image will be reduced, and the resolution of each layer of the pyramid will be reduced by a fixed ratio, as shown in Fig. 2(a).

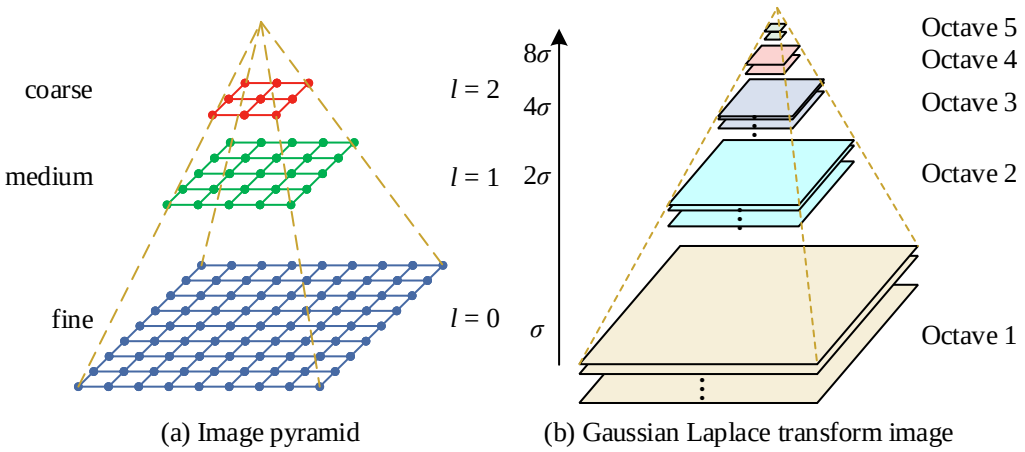

(a) Image pyramid (b) Gaussian Laplace transform image

Figure 2: Two kinds of transformed images in the SIFT algorithm

The Gaussian Laplace transform image (LOG image) is obtained by fusing the two methods. The specific method is to add photos at different blurring levels to each layer of the original image pyramid, as shown in Fig. 2(b). Subtracting the neighboring images of each layer on the basis of the LOG image to get all the reconstructed pyramids is the Difference of Gaussian Pyramid (DOG pyramid), and all the feature points are extracted on the DOG pyramid in the later stage.

(2) Determination of key point location

Thresholding is performed on all pixel points to filter out the noisy and unstable points in them. See expression (5) for details.

$$abs(val) > 0.5 * T / n \tag{5}$$

$T = 0.04$, an empirical value; n is the number of layers in which the feature points are wanted to be extracted.

Each pixel point is compared with its surrounding eight pixel points and the nine pixel points in the upper and lower layers, and when it is greater or less than all the neighboring points, it is determined to be an extreme point. A Taylor expansion is performed on the detected extreme points to determine the exact location of the extreme point, and the exact extreme point is obtained by solving the partial derivative of the expansion equation and making the derivative zero.

(3) Assigning directions to key points

The gradient direction and gradient magnitude of all pixels within a circle of 1.5 times the radius of the Gaussian image scale where the feature point is located are counted with the feature point as the center of the circle, and the angle of the gradient direction is the scale of the horizontal axis, and if 45 degrees is taken as a unit, there are eight scales in the horizontal axis, and the vertical axis is the cumulative value of the corresponding gradient assignment. Take the direction with the highest amplitude to determine the main direction, and when there is a second peak will be more than eighty percent of the peak capacity of the direction, called the auxiliary direction.

2.2.2 Feature Point Matching Algorithm

Constructs descriptors for the identified feature points. Divide the neighborhood of a specified range near the feature point into a grid of specified regions and rotate the x-axis of the original image to the same direction as the principal direction. In each divided grid region, there are

histograms of the gradient directions in eight directions, and the cumulative value of each gradient direction is plotted to form a seed point. Unlike when solving for the main direction of the feature point, at this time, the histogram of gradient direction of each subregion divides 0~360 degrees into eight direction ranges, each direction range is 45 degrees, then each seed point is endowed with the gradient intensity information of eight directions. There are 16 sub-regions, each containing 8 dimensional information, forming a 128-dimensional SIFT feature vector. The feature vectors are Gaussian weighted, and the weighting is performed using a standard Gaussian function with a variance of 1.5σ, and the distance is set to the distance of each point with respect to the feature point, and the best match is determined by traversing the descriptors of all the feature points in the two images.

3 Machine Vision Based Stress Calculation and Deflection Measurement for Bridges

3.1 Calculation of bridge stress distribution based on finite element structural analysis

Before the bridge overall lifting construction, finite element simulation simulation analysis of the lifting process is carried out to pre-check the deformation and internal force distribution of the bridge. In this paper, the traditional method is changed, and the finite element structural analysis method is organically combined with the image measurement algorithm based on machine vision, and the real-time position change information of the key points of the bridge, Δx_i and Δy_i, obtained by the image measurement algorithm based on machine vision, are used as the boundary condition information in the process of the finite element analysis of the bridge and analyzed, so that it can be realistically and efficiently real-time access to the overall stress distribution data during the overall lifting process of the bridge.

According to the basic theory of finite element, equations (6)-(7) can be obtained:

$$K\Delta = R \tag{6}$$

$$\sigma = DBG\Delta \tag{7}$$

where: K is the overall stiffness matrix of the bridge; Δ is the overall equivalent node displacement vector; R is the overall equivalent node load vector; σ is the stress matrix of the unit; D is the elasticity matrix; B is the strain matrix; G is the position matrix.

Static analysis of the bridge structure, the bridge for the horizontal state, so the calculation of internal forces only need to consider the wind load and the structure of the self-weight load; and the actual construction, the impact of the bridge hydraulic lifting process of the overall stress distribution of the factors also include the two sides of the lifting point lifting speed caused by the bridge tilted to the relative position of the key node changes. The image measurement algorithm based on machine vision can provide this kind of relative position change information of key nodes in real time, calculate the displacement information of all key nodes at a certain lifting moment, take the left (or right) end node as the reference node, and further calculate the relative position change information of all key nodes as in Eq. (8).

$$\left(\Delta x_i^r, \Delta y_i^r\right) = \left(\Delta x_r - \Delta x_i, \Delta y_r - \Delta y_i\right) \tag{8}$$

where: $\left(\Delta x_i^r, \Delta y_i^r\right)$ is the relative position change information of node i; Δx_i and Δy_i are

the position change information of node i; Δx_r and Δy_r are the position change information of the reference node.

The relative position change information of the key nodes of the bridge at the moment of t obtained by Eq. (8) is brought into Eqs. (6) and (7) for finite element analysis, and the stress distribution of the bridge as a whole at the moment of t can be obtained.

3.2 Machine Vision Based Bridge Deflection Measurement

3.2.1 Camera baseline distance and angle field adjustments

When 3D deflection inspection of bridge structure is carried out on site, due to the limitation of site conditions, it is generally necessary to adjust the baseline distance between binocular cameras, the angle between two cameras or replace the camera lens on site in order to balance the contradiction between the field of view of the measurement system and the inspection resolution. After adjusting the baseline distance, camera angle or replacing the lens, the internal and external parameters of the binocular camera are calculated for the subsequent 3D deflection measurement.

3.2.2 Three-dimensional deformation output

The 3D deformation information of the structure surface can be obtained by subtracting the 3D coordinates output from the measurement process at different moments as in equation (9):

$$\begin{cases} u = X_{w,t_n} - X_{w,t_0} \\ v = Y_{w,t_n} - Y_{w,t_0} \\ w = Z_{w,t_n} - Z_{w,t_0} \end{cases} \tag{9}$$

In Eq. (9), u, v and w correspond to the deformation in the X_w, Y_w and Z_w directions, respectively.

4 Stress calculation and deflection monitoring of bridges under asymmetric loading

4.1 Stress Observation and Calculation Based on Asymmetric Loads on Bridges

4.1.1 Calculation of asymmetric loads

During the cantilever construction of a bridge, prestressed tensioning is carried out. To effectively bond the prestressed tendons with the structural concrete and protect the steel bundles from rusting, grouting and filling are conducted in the prestressed ducts after tensioning the steel bundles. Generally, single-end grouting is carried out, and for Bridges with longitudinal slopes, low-end grouting (low in and high out) is chosen. During the grouting operation, due to improper operation by workers or weak safety awareness, It is possible that all the required grouting materials will be piled up at one end of the bridge deck grouting side, which will subject the cantilever structure to asymmetric loads and affect the force and displacement of the bridge. In this paper, based on the River Gorge Bridge K, a machine vision-based image measurement algorithm is used to obtain real-time change

information on the location of the key points of the bridge cantilever structure, and the effect is analyzed by finite element calculation.

The weight of the unit grout multiplied by the length of the aperture is the weight of the asymmetric load at the block section. Considering that the grout may not be placed all over the bridge deck slab during the actual construction, the maximum load is multiplied by the coefficients, i.e., 95%, 85%, 75%, and 65%, to discuss the effect of different sizes of asymmetric loads on the continuous rigid bridge. The specific load values obtained from the calculations are shown in Table 1.

Table 1: Unsymmetrical load(kN)

		Weight				
		100%	95%	85%	75%	65%
Blocksegment	1	56.7	51.2	45.6	40.0	34.4
	2	72.0	64.9	57.8	50.7	43.6
	3	87.9	79.2	70.5	61.8	53.1
	4	103.6	93.3	83.1	72.8	62.5
	5	119.4	107.6	95.7	83.9	72.0
	6	137.9	124.2	110.5	96.8	83.1
	7	156.4	140.8	125.3	109.7	94.2
	8	174.9	157.5	140.1	122.7	105.3
Cross segment	9	193.1	173.9	154.7	135.4	116.2
	10	211.1	190	169	148	127
	11	232.2	209.1	185.9	162.8	139.6
	12	253.4	228.2	202.9	177.7	152.4
	13	274.7	247.3	219.9	192.5	165.1
	14	295.8	266.3	236.8	207.3	177.8
	15	316.7	285.1	253.5	221.9	190.3

4.1.2 Stress observation data processing and calculations

According to the burial of the stress measurement points of the K Bridge, the stress condition inside the box girder during the actual construction condition is measured as (V2) measured value using the image measurement algorithm based on machine vision. The 20 construction blocks under the buried 3 important nodes (1-3) are selected, and the difference between the calculated value of stress at the top plate of the control section of the bridge (V1), the measured value of (V2) and (V3) is shown in Table 2, and the difference between the calculated value of stress at the bottom of the cross-section (V1), the measured value of (V2) and (V3) is shown in Table 3.The stresses in the table are all positive in tensile stress and negative in compressive stress.

Table 2: The comparison between the calculated factual stresses of top plane(MPa)

	Node 1			Node 2			Node 3		
	V1	V2	V3	V1	V2	V3	V1	V2	V3
1	-1.58	-0.45	1.13	-1.63	-0.53	1.1	-1.65	-0.55	1.1
2	-2.84	-0.98	1.86	-2.9	-1.05	1.85	-2.96	-1.09	1.87
3	-4.05	-2.2	1.85	-4.12	-2.26	1.86	-4.16	-2.32	1.84
4	-5.18	-3.31	1.87	-5.26	-3.4	1.86	-5.31	-3.47	1.84
5	-6.27	-4.4	1.87	-6.34	-4.48	1.86	-6.4	-4.56	1.84
6	-7.26	-5.4	1.86	-7.34	-5.49	1.85	-7.41	-5.58	1.83
7	-8.23	-6.34	1.89	-8.29	-6.43	1.86	-8.36	-6.47	1.89
8	-9.1	-7.25	1.85	-9.17	-7.32	1.85	-9.22	-7.38	1.84
9	-9.96	-8.09	1.87	-10.02	-8.17	1.85	-10.08	-8.24	1.84
10	-10.57	-8.72	1.85	-10.63	-8.79	1.84	-10.7	-8.88	1.82
11	-11.11	-9.25	1.86	-11.17	-9.33	1.84	-11.22	-9.39	1.83
12	-11.71	-9.73	1.98	-11.64	-9.8	1.84	-11.58	-9.86	1.72
13	-12.11	-10.13	1.98	-12.04	-10.22	1.82	-11.99	-10.28	1.71
14	-12.49	-10.54	1.95	-12.41	-10.6	1.81	-12.34	-10.67	1.67
15	-12.85	-10.87	1.98	-12.77	-10.95	1.82	-12.71	-11.01	1.7
16	-13.14	-11.2	1.94	-13.07	-11.26	1.81	-13.01	-11.32	1.69
17	-13.4	-11.45	1.95	-13.32	-11.52	1.8	-13.24	-11.58	1.66
18	-13.86	-11.94	1.92	-13.56	-11.77	1.79	-13.71	-12.06	1.65
19	-13.86	-11.94	1.92	-13.79	-12	1.79	-13.71	-12.06	1.65
20	-14.09	-12.42	1.67	-14.21	-12.16	2.05	-13.85	-12.3	1.55

Table 3: The comparison between the calculated factual stresses of bottom plane(MPa)

	Node 1			Node 2			Node 3		
	V1	V2	V3	V1	V2	V3	V1	V2	V3
1	-1.14	-0.49	0.65	-1.09	-0.42	0.67	-1.05	-0.41	0.64
2	-1.56	-0.92	0.64	-1.51	-0.84	0.67	-1.46	-0.79	0.67
3	-2.04	-1.39	0.65	-1.99	-1.32	0.67	-1.94	-1.30	0.64
4	-2.57	-1.92	0.65	-2.52	-1.85	0.67	-2.46	-1.83	0.63
5	-3.16	-2.50	0.66	-3.11	-2.44	0.67	-3.05	-2.41	0.64
6	-3.79	-3.15	0.64	-3.74	-3.07	0.67	-3.70	-3.04	0.66
7	-4.45	-3.81	0.64	-4.40	-3.73	0.67	-4.34	-3.69	0.65
8	-5.32	-4.66	0.66	-5.25	-4.59	0.66	-5.20	-4.57	0.63
9	-6.21	-5.58	0.63	-6.16	-5.50	0.66	-6.11	-5.49	0.62
10	-7.06	-6.53	0.53	-7.13	-6.46	0.67	-7.20	-6.39	0.81
11	-8.07	-7.52	0.55	-8.13	-7.47	0.66	-8.21	-7.40	0.81
12	-9.08	-8.55	0.53	-9.16	-8.50	0.66	-9.22	-8.45	0.77
13	-10.13	-9.59	0.54	-10.20	-9.54	0.66	-10.28	-9.47	0.81
14	-11.35	-10.68	0.67	-11.28	-10.62	0.66	-11.21	-10.56	0.65
15	-12.45	-11.76	0.69	-12.38	-11.72	0.66	-12.30	-11.65	0.65
16	-13.55	-12.89	0.66	-13.50	-12.84	0.66	-13.42	-12.77	0.65
17	-14.67	-14.03	0.64	-14.62	-13.96	0.66	-14.55	-13.89	0.66
18	-15.36	-14.74	0.62	-15.30	-14.63	0.67	-15.21	-14.60	0.61
19	-16.34	-15.63	0.71	-16.26	-15.13	1.13	-16.05	-15.41	0.64
20	-17.39	-16.12	1.27	-17.28	-15.67	1.61	-17.09	-16.00	1.09

Based on the graphs in Table 2 and Table 3, the calculated and machine vision measured stresses in the top and bottom plates at the maximum cantilever stage of the project are shown in Fig. 3, from which it can be seen that the stresses in the top and bottom plates at the root of the cantilever at the maximum cantilever stage of the Bridge K have reached the maximum value, and the majority of the girder segments are in the state of compression. The calculated maximum stress of the top plate is 14.18 MPa, and the measured maximum stress is 14.62 MPa. The calculated maximum stress of the bottom plate is 17.49 MPa, and the measured maximum stress is 17.91 MPa. The error between the calculated data and the measured data is controlled within the interval of (0.00,0.50), which is not much different from each other, and is in line with the requirements.

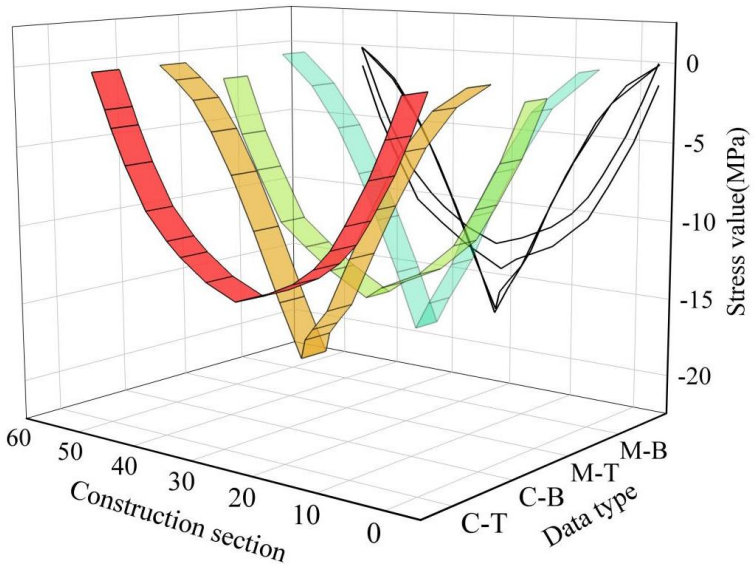

Figure 3: The calculated and factual stresses of the cantilever of top and bottom plates

4.2 Machine Vision Based Bridge Deflection Monitoring

4.2.1 Field calibration of bridges

In order to verify the actual performance of the measurement system equipped with the machine vision image measurement algorithm in this paper, a field calibration test was conducted on the K-bridge bridge. The measurement system measures the interval displacement between 2 LEDs with working distances of 300, 550 and 900m respectively. When the two LEDs are fully illuminated, the difference between the two displacement coordinates at the same time is the distance between the two; when one of the LEDs is off, the difference between the displacement coordinates of the other illuminated LED at the same time is 0. The results of the on-site calibration test for the three kinds of working distances are plotted in Fig. 4 for the sampling frequencies of 5 Hz and 25 Hz. The data on the left side of the data labels in the figure are the interval distances, and the data on the right side are the sampling frequency, for example, (300,5) is the measurement result of 300m working distance under 5Hz. On the whole, the measured value and the actual value of the measurement system under machine vision are highly consistent, and the measurement error is not more than 5mm at a working distance of hundreds or even thousands of meters, and the measurement error increases with the increase of the working distance; the higher the sampling frequency, the smaller the measurement error at the same working distance.

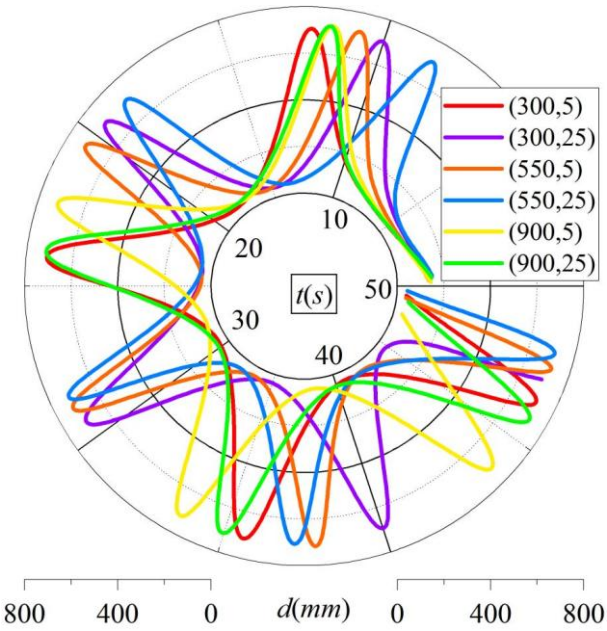

Figure 4: On-site calibration test

4.2.2 Analysis of Deflection Measurement Results

The state when the bridge is not loaded with weights is taken as the initial state, and the three-dimensional coordinates of the identification points of this state are reconstructed. The three-dimensional coordinates obtained from the ten times of data collected in the first state are used to find a center of gravity, which is used as the initial reference value. With the traditional deflection measurement method micrometer as a control, through this paper deflection measurement method measured by 150 sets of data and micrometer measured data comparison is shown in Figure 5, the dark blue curve in the figure for the micrometer measured data, light blue for the method of this paper measured data, light blue filled area for the difference between the two data. It can be seen that the deflection trend of the two data is consistent, the data values are within the (0.5,3.0) interval, and the error area between the data is small.

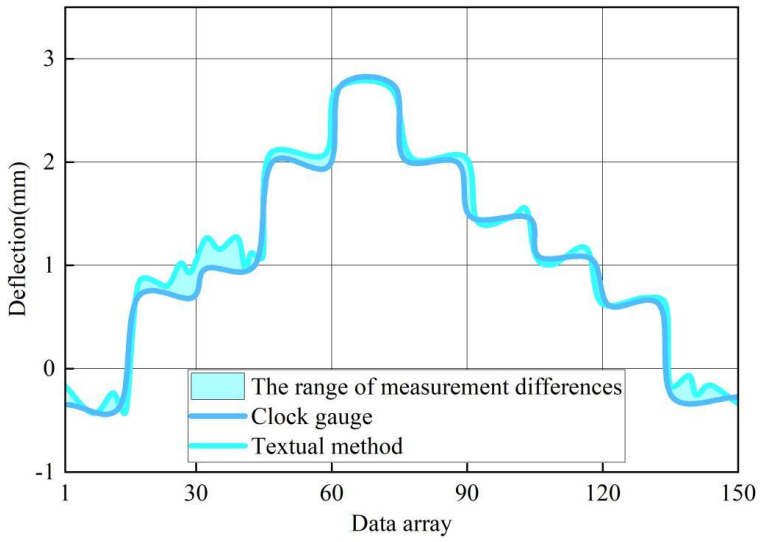

Figure 5: Comparison of deflection measurement

4.2.3 Mid-span deflection monitoring of large bridges

The time-domain curve of the vertical deflection of the bridge span of K Bridge between 19:00 and 19:32 of a certain day based on machine vision and the GPS method is shown in Fig. 6, and the frequency spectrum curve is shown in Fig. 7. Comprehensively observing Fig. 6 and Fig. 7, it is found that the synchronized measurement results of the bridge deflection based on machine vision and the GPS method for the bridge span vertical deflection are highly consistent in the time-domain and the frequency domain, The difference is less than 1mm, and the maximum value of the vertical deflection of the bridge span is 924.77mm in the measurement time period.

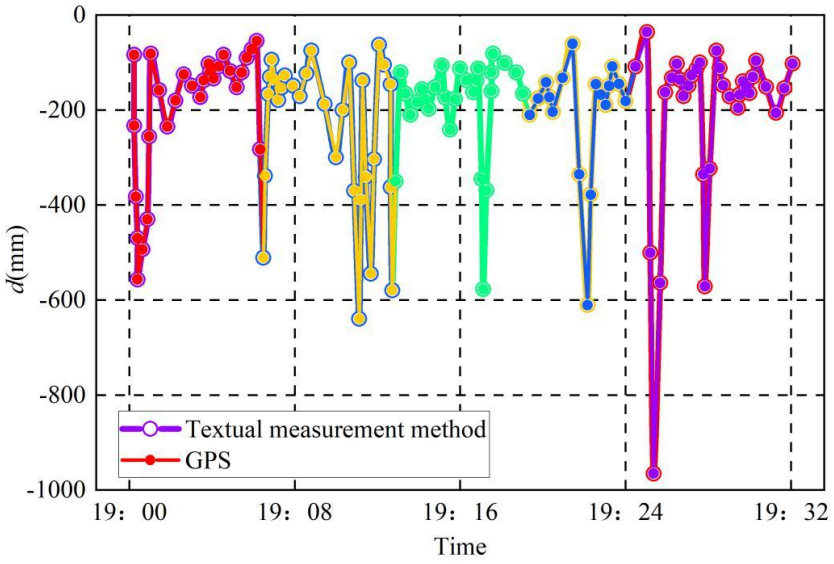

Figure 6: The time-domain curve of the mid-span deflection of a bridge

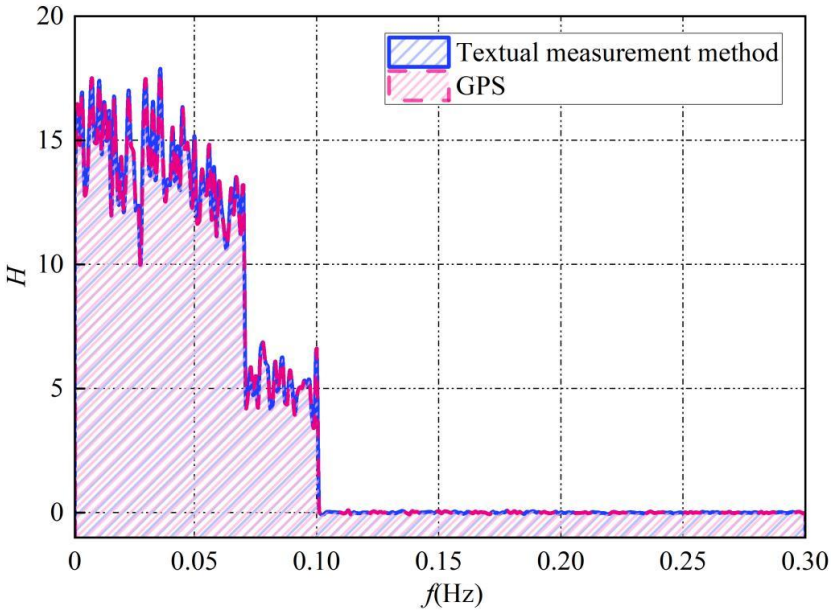

Figure 7: The spectral curve of the mid-span deflection of the bridge

5 Conclusion

In this paper, an image measurement algorithm based on machine vision is proposed by synthesizing image distortion correction under camera calibration and SIFT-based feature point monitoring and matching algorithm. With the technical support of this algorithm, a finite element structural analysis method of bridge stress distribution and a bridge deflection measurement method are constructed. Under the application conditions of asymmetric loading of the bridge, the maximum stress of the bridge cantilever top plate is 14.18MPa and the maximum stress of the bottom plate is 17.49MPa, and the difference with the measured data is less than 0.50. In the field calibration, the measurement error is always less than 5mm under the conditions of various working distances and sampling frequencies. For the bridge deflection measurement data, it is not only similar to the micrometer measurement method, but also differs from the GPS method by <1mm, and the maximum value of the vertical deflection of the bridge span in the measurement time period is 924.77mm.The image measurement algorithm based on machine vision realizes the real-time measurement of the stress and deflection under the asymmetric load of the bridge through higher measurement accuracy and lower measurement cost.

References

[1] Mishra, A. K. (2018). Practices for quality management system adopted in the bridge construction projects of Kathmandu, Nepal. J Adv Res Qual Control Mgmt, 3(1&2), 42-52.

[2] Zhang, G., & Li, H. (2024). Road and Bridge Construction Technology and Quality Control Measures and Analysis. Journal of Theory and Practice of Management Science, 4(03), 6-11.

[3] Fairclough, H. E., Gilbert, M., Pichugin, A. V., Tyas, A., & Firth, I. (2018). Theoretically optimal forms for very long-span bridges under gravity loading. Proceedings of the Royal Society A: Mathematical, Physical and Engineering Sciences, 474(2217), 20170726.

[4] Liu, T., Fan, J., & Peng, Z. (2022). Central load-bearing control in the construction process of the concrete spherical joint nandu river swing bridge: a case study. Buildings, 12(5), 511.

[5] Sobczyk, B., Pyrzowski, Ł., Miśkiewicz, M., Chróścielewski, J., & Wilde, K. (2025). Impact assessment of excessive and undesirable deformations in cable-to-girder connections on the structural safety of the University cable-stayed bridge in Bydgoszcz (Poland). Engineering Failure Analysis, 171, 109400.

[6] Hraib, F., Hui, L., Vicente, M., & Hindi, R. (2019). Evaluation of bridge exterior girder rotation during construction. Engineering Structures, 187, 149-160.

[7] Huang, Q., Wu, X., Zhang, Y., & Ma, M. (2022). Proposed new analytical method of tower load in large-span arch bridge cable lifting construction. Applied Sciences, 12(18), 9373.

[8] Yu, J., Zhang, J., Li, P., & Han, X. (2023). Influence of Superstructure Pouring Concrete Volume Deviation on Bridge Performance: A Case Study. Buildings, 13(4), 887.

[9] Huang, K., Jin, H., Xu, Y., & Zhou, J. (2025). Blast-resistance performance of bridge jacking support subjected to up-deck blast load. KSCE Journal of Civil Engineering, 100382.

[10] He, Z. Q., Ma, Z., Zhang, S., Liu, Z., & Ma, Z. J. (2021, October). Temperature gradients and stress distributions in concrete box-girder bridges during hot-mix asphalt paving. In Structures (Vol. 33, pp. 1954-1966). Elsevier.

[11] Wang, Y., Chen, Z., & Qi, Y. (2023). Research on the impact of irregular structure group construction on rail transit bridge piers and its response to wind load. Scientific reports, 13(1), 10469.

[12] Wu, H., Yang, Z., Lu, C., Li, Z., Guo, C., & Sha, G. (2024). Study on the Stability of Unbalanced Rotation of Large-Tonnage T-Shaped Rigid Frame Bridges. Buildings, 14(12), 3927.

[13] Wang, Y., Wang, B., Li, C., Zheng, F., Liu, Y., & He, S. (2025). Construction Monitoring and Analysis of Asymmetric Prestressed Concrete Bridge Crossing Multiple-Line Railways. Structural Durability & Health Monitoring (SDHM), 19(2).

[14] Li, T., Cong, B., Yan, M., Li, Q., & Zhu, X. (2023). Safety BIM intelligent modeling analysis of prestressed concrete continuous girder bridge construction scene. Bridge Structures, 19(1-2), 31-39.

[15] Gaute-Alonso, A., Garcia-Sanchez, D., Ramos-Gutierrez, Ó. R., & Ntertimanis, V. (2024). Enhancing stress measurements accuracy control in the construction of long-span bridges. Scientific Reports, 14(1), 10961.

[16] Zheng, X., Li, D., Zhang, K., Xue, X., & Min, F. (2023). CONSTRUCTION VERIFICATION OF UNDER-BEARING ARCH BRIDGE BASED ON CONSTRUCTION MONITORING AND TEST. Stavební obzor-Civil Engineering Journal, 32(3), 298-313.

[17] Zhang, C., Ge, Y., Hu, Z., Zhou, K., Ren, G., & Wang, X. (2019). Research on deflection monitoring for long span cantilever bridge based on optical fiber sensing. Optical Fiber Technology, 53, 102035.

[18] Moru, D. K., & Borro, D. (2020). A machine vision algorithm for quality control inspection of gears. The International Journal of Advanced Manufacturing Technology, 106(1), 105-123.

[19] Smith, M. L., Smith, L. N., & Hansen, M. F. (2021). The quiet revolution in machine vision-a state-of-the-art survey paper, including historical review, perspectives, and future directions. Computers in Industry, 130, 103472.

[20] Frustaci, F., Spagnolo, F., Perri, S., Cocorullo, G., & Corsonello, P. (2022). Robust and high-performance machine vision system for automatic quality inspection in assembly processes. Sensors, 22(8), 2839.

[21] Zhao, Y., Wang, Z., Liu, J., & Zhang, B. (2025). Machine vision-based technology for the interface classification of precast concrete components. Engineering Structures, 329, 119835.

[22] Dan, D., Ying, Y., & Ge, L. (2021). Digital twin system of bridges group based on machine vision fusion monitoring of bridge traffic load. IEEE Transactions on Intelligent Transportation Systems, 23(11), 22190-22205.

[23] Zhao, Q., Hu, C., Xia, G., & Chen, Y. (2024). Research of highway bridge settlement monitoring technology based on machine vision. J Res Sci Eng, 6(7), 29-32.

[24] Xie, H., Liao, Q., Liao, L., & Qiu, Y. (2024). Machine Vision-Based Real-Time Monitoring of Bridge Incremental Launching Method. Sensors, 24(22), 7385.